

NUMERICAL ANALYSIS OF ROTARY SWAGING OF STEERING TUBE

KUNČICKÁ Lenka¹, KOCICH Radim¹, JANOVSÁKÁ Kamila², POLCAR Luboš³, VEČERĚK Tomáš¹

¹Department of Materials Forming, VSB - Technical University of Ostrava, Ostrava, Czech Republic, EU, lenka.kuncicka@vsb.cz, radim.kocich@vsb.cz, tomas.vecerek.st@vsb.cz

²Department of Economics and Management in Metallurgy, VSB - Technical University of Ostrava, Ostrava, Czech Republic, EU, kamila.janovska@vsb.cz

³Department of Thermal Engineering, VSB - Technical University of Ostrava, Ostrava, Czech Republic, EU, lubos.polcar.st@vsb.cz

Abstract

Owing to its versatility and the ability to provide the final products with advantageous characteristics, rotary swaging is widely used in automotive industry for production of various components. The focus of this study was to perform numerical prediction of rotary swaging of a steering tube. The predicted results were subsequently evaluated with data gained from experimental swaging. The analyses carried out on the experimentally swaged model included measurements of microhardness, as well as scanning electron microscopy observations. To evaluate reliability of the simulation, the simulated swaged component was compared with a 3D-scanned real product. As shown by the results, the parameters of the dies and processing conditions defined in the simulation corresponded very well with the real process and thus the designed numerical model can be considered as an accurate one. The swaged product featured a very smooth surface and small equiaxed grains, 80 % of which were smaller than 1 μm , with no prevalent grains orientation.

Keywords: Rotary swaging; automotive; numerical simulation; structure analysis; mechanical properties

1. INTRODUCTION

Rotary swaging (RS) is a forming technology widely used to produce rods, tubes and wires of various cross-sections. The principle of the technology lies in incremental imposing of strain into the formed material via a set of swaging dies through which the material is fed, which results in a very favourable stress state [1-3], as well as has favourable effects on microstructure and properties [4,5]. RS can be used to process a wide range of materials, from light-weight ones like magnesium [6], aluminium [7], and titanium [8], through heavier ones like copper [9], to composites [10] and refractory metals [11], and can be performed under cold, warm, and hot conditions. Being one of the severe plastic deformation (SPD) technologies, cold RS provides the processed materials with substantial increases in strength and hardness via imparting grain refinement [12], likewise other SPD methods, such as HPT (high pressure torsion) [13], and ECAP (equal channel angular pressing) and its modifications [14-16]. It also enables to produce final shape products and, therefore, makes the production process more economical from the viewpoints of expenses and time. Advantageous are also the very low roughness and shape differences of the final products.

Owing to the above mentioned advantages, RS has been widespread in the automotive industry [17]. The technology enables to form not only the external shape of the final product, but also possible internal shape features and grooves. Nevertheless, especially in the automotive, research and development advances inexorably and thus a combination of the manufacturing technology, such as RS, with numerical predictions via the finite element method (FEM) can be extremely favourable. The combination of RS and FEM has already been successfully applied e.g. by Tao et al. [18] to examine deformation behaviour of swaged bimetal tubes, Rong et al. [19] to analyse the infeed velocity of Mg billets on strain distribution within the swaged-product, Kocich et al. [20] to investigate deformation behaviour of a WNiCo alloy during cold swaging, and Moumi et al. [21] to analyse material flow during swaging.

The aim of this study was to numerically predict the deformation behaviour of a steering tube during cold rotary swaging. The study involved performance of a numerical simulation of cold swaging of a steering tube and the subsequent comparison of the result of numerical swaging and the real swaged product via 3D scanning. The investigation also involved metallographic evaluation of the real final product via scanning electron microscopy (SEM) and microhardness measurements.

2. EXPERIMENT

The steering tube was manufactured from steel, the composition of which is depicted in **Table 1**. This composition was input to the Forge NxT commercial simulation software as the original material of the billet.

Table 1 Chemical composition of the steering tube steel

element	C	Mn	Si	Cr	Ni	Mo	Al	S	P	Fe
wt. %	0.148	0.76	0.06	0.039	0.013	0.054	0.08	0.013	0.015	balance

The assembly for the Forge NxT simulation, which is depicted in **Figure 1a**, consisted of the steel billet, four swaging dies, an internal mandrel and a clamp bar, which served to feed the work-piece further into the swaging head each time the dies were in the open position. During swaging, all the dies oscillated along the radial direction and simultaneously rotated around the swaging head axis after each stroke according to the input boundary conditions. The RS assembly was meshed using tetrahedron elements and the work-piece mesh consisted of 30 280 elements. The initial temperature of all the assembly components was 20 °C and the friction between the work-piece and dies was set using the Coulomb law, $\mu = 0.1$. The material behaviour was determined using a constitutive elastic-viscoplastic characterized by the Hensel-Spittel relation (Equation (1)), where ε (-) was the equivalent strain, $\dot{\varepsilon}$ (s⁻¹) was the equivalent strain rate, T (K) was the temperature and A, m_1 , m_2 , m_3 , m_4 , m_5 , m_7 , m_8 , m_9 were regression coefficients (-), the values of which were the following: A=885.92, $m_1=-0.009$, $m_2=0.157$, $m_3=0.0099$, $m_4=0.0003$, m_5 , m_7 , m_8 , m_9 were 0.

$$\sigma = A \exp(m_1 T) T^{m_2} \varepsilon^{m_3} \exp\left(\frac{m_4}{\varepsilon}\right) (1 + \varepsilon)^{m_5} \exp(m_7 \varepsilon) \dot{\varepsilon}^{m_8} \varepsilon^{m_9} \quad (1)$$

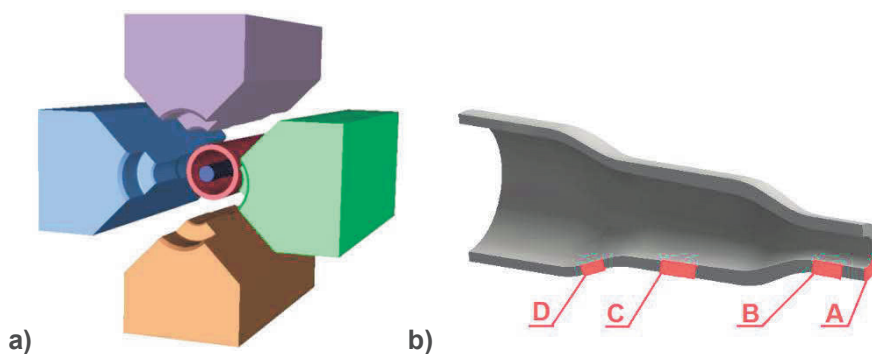


Figure 1 Numerical analysis assembly (a); depiction of locations for the individual analyses (b)

The numerically predicted shape was subsequently compared with a 3D scan of the real swaged product. After the 3D scan had been taken, four samples from four different locations denoted as A, B, C and D, as depicted in **Figure 1b**, were taken from the swaged-piece for subsequent microstructural and microhardness analyses. The microhardness was measured using a Vickers diamond indenter with the load of 400 g, measurements were performed ten times in each of the locations and the average values for the individual locations were subsequently calculated. The structural observations were performed with an Olympus optical microscope and Tescan Lyra 3 FIB/SEM with a NordlysNano EBSD detector.

3. RESULTS AND DISCUSSION

3.1. FEM Analysis

3.1.1. Effective strain

The following set of Figures summarizes the results of the numerical prediction. **Figure 2a** shows the predicted distribution of the effective strain within the swaged steering tube. Evidently, the imposed strain was the highest in the part, in which the reduction in diameter was the most significant. The strain on the perimeter of the swaged-piece in this location exceeded 1.5, while on the internal diameter it was around ~ 0.6 . **Figure 2b** then depicts the imposed strain (in)homogeneity by showing the time dependence of the imposed strain in seven individual locations characterized by sensors located along the central cutting plane as shown in **Figure 2c**. The inhomogeneity across the diameter is given by the radial character of imposing strain during swaging [1,22].

3.1.2. Temperature

As shown by the results of temperature prediction depicted in **Figure 2d**, the maximum temperature reached to 200 °C and the region, in which the temperature was the highest, corresponded to the region with the highest imposed strain. This corresponds to the fact that most of the energy introduced into the material during forming (up to 98 %) is transformed to heat and, therefore, the most intensive energy input resulted in the highest increase in temperature [23].

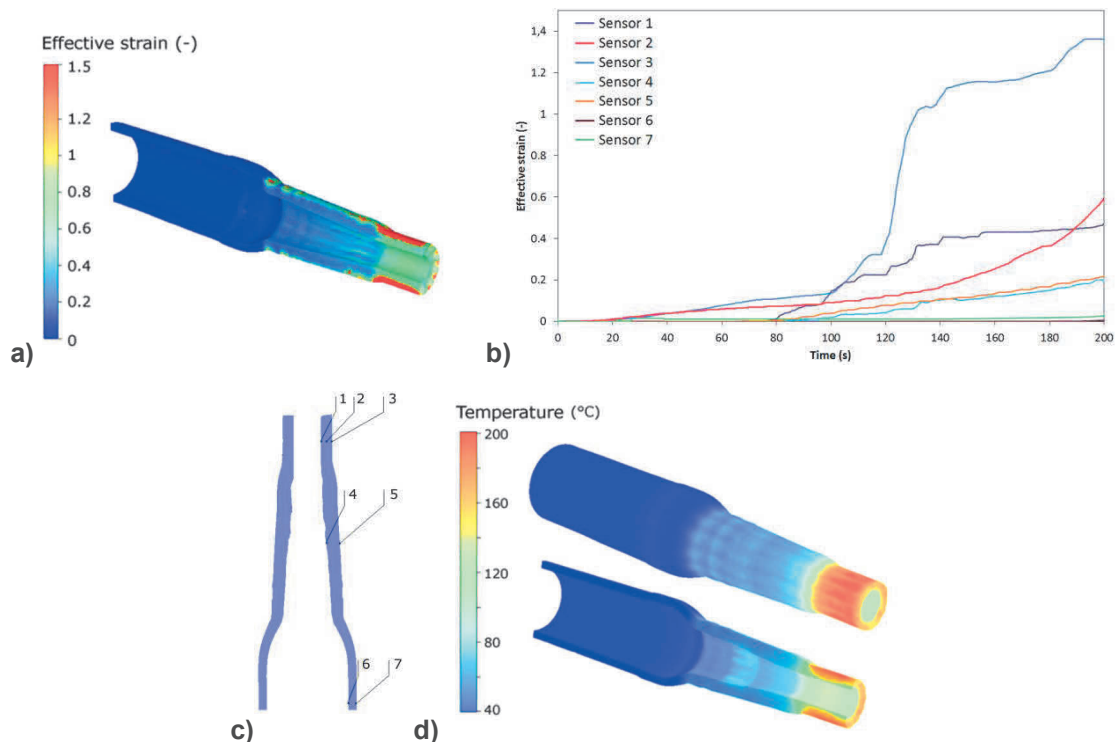


Figure 2 Predicted imposed strain within the steering tube (a); imposed strain in individual locations along the steering tube central cutting plane (b); locations of sensors (c); temperature distribution (d)

3.1.3. Material flow

Figure 3a shows a grid superimposed on the initial billet central cutting plane, while **Figure 3b** depicts the grid after swaging. Evidently, the thickness of the final tube increased in many locations, which was caused by the mandrel having a lower diameter than the final internal one of the tube in the concrete locations (the mandrel

was insert to maintain accurate dimension of the outlet part of the steering tube and did not perfectly reproduce the shape of the steering tube). The predominant axial material flow typical for rotary swaging [21] was thus in this case suppressed by the tendency of the material to flow towards the axis of the work-piece.

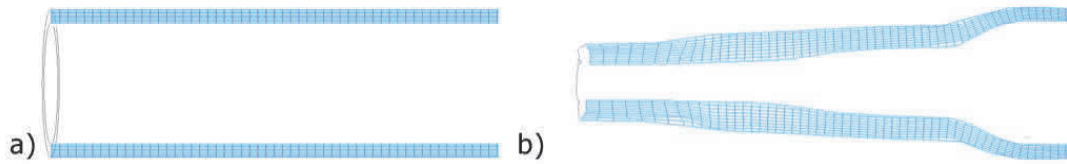


Figure 3 Predicted material flow

3.2. Comparison with real product

To validate the numerical model and evaluate the accuracy of the simulation, the predicted swaged-piece was compared with the real steering tube (**Figure 4a**) scanned using a 3D scanner. The final comparison with a scale showing the deviation between the predicted and real part in (mm) is shown in **Figure 4b**. The model was highly accurate since the deviations between the real and simulated part was in tenths of millimetre (the high deviation at the very end of the component corresponded to the hollow character of the component).

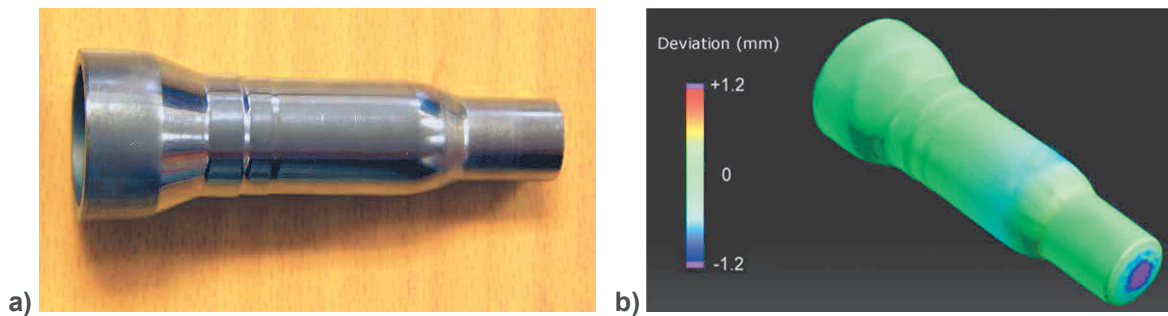


Figure 4 The real steering tube (a); comparison of the real 3D scan and predicted swaged-piece (b)

3.3. Experimental analyses

3.3.1. Microhardness

The average microhardness in the individual locations *A*, *B*, *C* and *D* is summarized in **Table 2**. Location *D* exhibited the least imposed strain (close to 0 - **Figure 1b**), and can thus be considered as the original undeformed material, which featured the microhardness of almost 200 HV. Locations *B* and *C* both experienced the effect of strain, however, location *B* was affected by strain more and, correspondingly, also featured higher microhardness. The direct connection between the predicted imposed strain and changes in microhardness was already mentioned in various works [16, 24]. Microhardness in location *A* was lower than in locations *B* and *C*. HV for location *A* was measured in a different direction (perpendicular cut, while the others were longitudinal ones), at the very end of the steering tube. For this location, the axial plastic flow was the easiest and the impact of the dies during swaging was lower than the impact on the material along the perimeter of the steering tube, on which the effect of the dies was direct.

Table 2 Average microhardness in the individual locations depicted in **Figure 1b**

Sample	A	B	C	D
Avg. HV	217.76	232.98	225.42	199.56

3.4. Grain size

The average grain size, calculated as the mean ferret diameter of an individual grain in μm , in the individual locations *A*, *B*, *C* and *D* are summarized in **Table 3**. The grains got evidently refined the more the higher was the imposed strain. Correspondingly, grain refinement imparted increase in microhardness, as proven in Section 3.1. The finest grains, 80 % of which were smaller than 1 μm , were detected in location *A*, however, this was caused by the direction of measurement (perpendicular cut). **Figure 5** then shows an example of the microstructure of the swaged material from location *B* via an orientation image map. The grains did not exhibit any prevalent preferential orientation and were evidently refined, which was the result of the mutual influence of the imposed strain, friction between the swaged-piece and dies and consequent temperature elevation [25].

Table 3 Average grain size in the individual locations depicted in **Figure 1b**

Sample	A	B	C	D
Avg. grain size	1.12	2.67	3.36	4.75

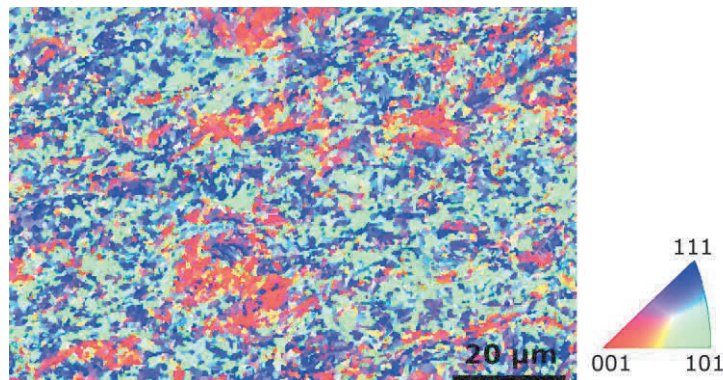


Figure 5 OIM of location B

4. CONCLUSIONS

This study dealt with numerical prediction of cold rotary swaging of a steering tube. From the simulation, the distribution of imposed strain, temperature and plastic flow were evaluated. The locations with the highest imposed strain of almost 1.5 corresponded to the locations of the highest temperature of almost 200 °C. The results from experimental analyses confirmed the predicted results; the most heavily deformed region exhibited the highest microhardness of more than 230 HV, as well as the lowest average grain size. The numerical model was finally evaluated via a comparison with a 3D-scanned real steering tube. The comparison showed the deviation of the predicted and real components to be within tenths of millimetre.

ACKNOWLEDGEMENT

This paper was created within the research project no. SP2017/58, "Specific research in metallurgical, material, and process engineering".

REFERENCES

- [1] KOCICH, R., et al. Deformation behavior of multilayered Al-Cu clad composite during cold-swaging. *Materials and Design*, 2016, vol. 90, pp. 379-388.
- [2] PIWEK, V., et al. Light weight design of rotary swaged components and optimization of the swaging process. *International Journal of Material Forming*, 2010, vol. 3, pp. 845-848.
- [3] HERRMANN, M., SCHENCK, C., KUHFUSS, B. Dry rotary swaging with structured tools. *Procedia CIRP* 2016, vol. 40, pp. 653-658.

- [4] GRÖB, T., et al. Magnetic hardening of Fe50Co50 by rotary swaging. *Journal of Magnetism and Magnetic Materials*, 2017, vol. 428, pp. 255-259. doi:10.1016/j.jmmm.2016.12.065.
- [5] ABDULSTAAR, M. Corrosion behaviour of Al 1050 severely deformed by rotary swaging. *Materials and Design*, 2014, vol. 57, pp. 325-329.
- [6] GAN, W.M., et al. Microstructures and mechanical properties of pure Mg processed by rotary swaging. *Materials and Design*, 2014, vol. 63, pp. 83-88.
- [7] ŞCHIOPU, V., LUCA, D. A new net-shape plating technology for axisymmetric metallic parts using rotary swaging. *International Journal of Advanced Manufacturing Technology*, 2016, vol. 85, pp. 2471-2482.
- [8] PACHLA, W., et al. Effect of severe plastic deformation realized by hydrostatic extrusion and rotary swaging on the properties of CP Ti grade 2. *Journal of Materials Processing Technology*, 2015, vol. 221, pp. 255-268.
- [9] OTTO, F., FRENZEL, J., EGGELER, G. On the influence of small quantities of Bi and Sb on the evolution of microstructure during swaging and heat treatments in copper. *Journal of Alloys and Compounds*, 2011, vol. 509, pp. 4073-4080.
- [10] KOCICH, R., et al. Fabrication and characterization of cold-swaged multilayered Al-Cu clad composites. *Materials and Design*, 2015, vol. 71, pp. 36-47.
- [11] DURLU, N., KANALISKAN, N., SAKIR, B. Effect of swaging on microstructure and tensile properties of W-Ni-Fe alloys. *International Journal of Refractory Metals and Hard Materials*, 2014, vol. 42, pp. 126-31.
- [12] GAN, W.M., et al. Bulk and local textures of pure magnesium processed by rotary swaging. *Journal of Magnesium and Alloys*, 2013, vol. 1, pp. 341-345.
- [13] KOCICH, R., et al. Texture, deformation twinning and hardening in a newly developed Mg-Dy-Al-Zn-Zr alloy processed with high pressure torsion. *Materials and Design*, 2016, vol. 90, pp. 1092-1099.
- [14] LUKÁČ, P., et al. Microstructure of AZ31 and AZ61 Mg alloys prepared by rolling and ECAP. *Kovové materiály-metallic materials*, 2007, vol. 45, pp. 115-20.
- [15] YOON, S.C., et al. Analysis of plastic deformation behavior during back pressure equal channel angular pressing by the finite element method. *Computational Materials Science*, 2013, vol. 77, pp. 202-207.
- [16] KOCICH, R., et al. Twist-channel angular pressing: effect of the strain path on grain refinement and mechanical properties of copper. *Journal of Materials Science*, 2011, vol. 46, pp. 7865-7876.
- [17] HASSELBRUCH, H. Incremental dry forging -Interaction of W-DLC coatings and surface structures for rotary swaging tools. *Procedia Manufacturing*, 2017, vol. 8, pp. 541-548.
- [18] TAO, S., et al. Plastic forming behavior of axisymmetric bimetal products with rotary swaging. *Engineering Sciences*, 2013, vol. 11, pp. 44-47.
- [19] RONG, L., NIE, Z.R., ZUO, T.Y. FEA modeling of effect of axial feeding velocity on strain field of rotary swaging process of pure magnesium. *Transactions of Nonferrous Metals Society of China (English Ed.)*, 2006, vol. 16, pp. 1015-1020.
- [20] KOCICH, R., et al. Cold rotary swaging of a tungsten heavy alloy: Numerical and experimental investigations. *International Journal of Refractory Metals and Hard Materials*, 2016, vol. 61, pp. 264-272.
- [21] MOUMI, E., et al. 2D-simulation of material flow during infeed rotary swaging using finite element method. *Procedia Engineering*, 2014, vol. 81, pp. 2342-2347.
- [22] ZHANG, Q., et al. Energy-controlled rotary swaging process for tube workpiece. *The International Journal of Advanced Manufacturing Technology*, 2015, vol. 80, pp. 2015-2026.
- [23] HUMPHREYS, F.J., HETHERLY, M. *Recrystallization and Related Annealing Phenomena*. 2nd ed. Oxford: Elsevier Ltd, 2004, p. 658.
- [24] DEL VALLE, J.A., CARRENO, F., RUANO, O.A. Influence of texture and grain size on work hardening and ductility in magnesium-based alloys processed by ECAP and rolling. *Materials Science and Engineering A*, 2013, vol. 48, pp. 190-195. doi:10.1016/j.msea.2006.05.009.
- [25] VERLINDEN, B., et al. *Thermo-mechanical processing of metallic materials*. Amsterdam: Elsevier, 2007, p. 560.